frontiers | Frontiers in Earth Science

TYPE Original Research
PUBLISHED 23 August 2022
DOI 10.3389/feart.2022.960358

Check for updates

OPEN ACCESS

EDITED BY
Zhuqi Zhang,
China Earthquake Administration, China

REVIEWED BY
Yuanze Zhou,
University of Chinese Academy of Sciences, China
Xiaobo Tian,
Institute of Geology and Geophysics (CAS), China
Zengxi Ge,
Peking University, China

*CORRESPONDENCE
Xuzhang Shen,
shenxzh5@mail.sysu.edu.cn

SPECIALTY SECTION
This article was submitted to Structural Geology and Tectonics, a section of the journal Frontiers in Earth Science

RECEIVED 02 June 2022
ACCEPTED 20 July 2022
PUBLISHED 23 August 2022

CITATION
Zhou Q, Shen X, Huang H, Cheng S and Zhang J (2022), Reworking of ancient tectonic amalgamation belt beneath the central north of North China Craton revealed by dense seismic observations. *Front. Earth Sci.* 10:960358. doi: 10.3389/feart.2022.960358

COPYRIGHT
© 2022 Zhou, Shen, Huang, Cheng and Zhang. This is an open-access article distributed under the terms of the Creative Commons Attribution License (CC BY). The use, distribution or reproduction in other forums is permitted, provided the original author(s) and the copyright owner(s) are credited and that the original publication in this journal is cited, in accordance with accepted academic practice. No use, distribution or reproduction is permitted which does not comply with these terms.

Reworking of ancient tectonic amalgamation belt beneath the central north of North China Craton revealed by dense seismic observations

Qiming Zhou[1,2], Xuzhang Shen[1,2]*, He Huang[1,2], Siyuan Cheng[1,2] and Jian Zhang[1,2]

[1]Guangdong Provincial Key Lab of Geodynamics and Geohazards, School of Earth Science and Engineering, Sun Yat-Sen University, Zhuhai, China, [2]Southern Marine Science and Engineering Guangdong Laboratory (Zhuhai), Zhuhai, China

The North China Craton (NCC) is one of the oldest cratons in the world, and its internal tectonic belt is often used to investigate the earth's tectonic evolution events. During the late Mesozoic and Cenozoic, the western Pacific subduction zone caused the restructuring of NCC by damaging the craton beneath eastern NCC, resulting in the distinct lateral differences between western and eastern NCC, which ultimately formed the current NCC. Furthermore, the subsequent tectonic events activated the ancient tectonic weak zones, and their traces are imprinted in the deep earth. Here, we investigated the crust structures with a high-density seismic array beneath the splice position of the eastern margin of the Khondalite Belt and the northern part of the central orogenic belt in NCC. The array included 140 short-period seismographs spaced at 2–3 km intervals, which recorded teleseismic three-component waveforms over a one-month period. P-wave receiver functions calculated from 25 teleseismic events provided an image of the crustal structure. The weak Moho and Moho offset under the study area are visible in the migration image of receiver functions. The geological investigations and the rock outcrops were combined to establish the strong coupling relationship between the present surface fault-depression system and deep structures. The deep material circulation, which governs the surface extension of the basin-range structure, is controlled by the deep material circulation which is ultimately derived from the continuous subduction of the western Pacific. The study's findings indicate that the ancient amalgamative belt might have transformed into a weak zone easily susceptible to modification by plate tectonic movements.

KEYWORDS

North China Craton, dense seismic observations, receiver function, weak zone, reworking

1 Introduction

Several tectonic events in the North China Craton (NCC) since the Archean have been documented, and the available geological evidence explains the various phases of NCC. Three major tectonic events that occurred during the late Paleoproterozoic were reported by many scholars (Kusky et al., 2016; Li S et al., 2015; Zhai and Santosh, 2011; Zhao et al., 2005, 2012, 2013). The western NCC (WNCC) was formed by the amalgamation of the Yinshan block and the Ordos block at ~1.95 Ga, while the eastern NCC (ENCC) was formed by the collision between Longgang and Nangrim blocks at ~1.90Ga. Furthermore, WNCC and ENCC amalgamated as a result of a tectonic event at ~1.85Ga to form the uniform basement of NCC along a central orogenic belt (Trans-North China Craton, TNCO) (Zhao et al., 2001; 2005). The NCC remained stable for a long time until the significant Mesozoic lithospheric thinning. Numerous ancient tectonic structures have been transformed due to the collision between India and Eurasia plates and the subduction of the Pacific plate, which resulted in the elevation of the Tibetan Plateau (Zhu et al., 2011; 2012). This indicates the vulnerability of the amalgamation belts to the subsequent tectonic disturbances. This Paleoproterozoic evolution process has also resulted in a unique tectonic background at the boundary between the eastern side of the Khondalite belt and the northern part of TNCO (Figure 1A). The central tectonic belt and Khondalite rock belt are connected along the Huai'an-Zhangjiakou area in Hebei province, China. The Shanxi–Hebei–Inner Mongolia basin tectonic belt, comprising a series of parallel Holocene faults and basins, characterizes the current surface structures and activities that are relatively distinctive (Figure 1B&c).The tectonic environment in the area is responsible for the relatively high tectonic activity (Li Z et al., 2015), as evidenced by the earthquake with ML = 6.2 triggered in Zhangbei in 1998 (Yang et al., 2002). The potential of this area for the occurrence of strong earthquakes is also evidenced by the GNSS observation data (Wu et al., 2021). The Huai'an-Zhangjiakou is a highly significant area of TNCO due to the area's paleotectonic and neotectonic activities. From northwest to southeast, the area comprises Yinshan block, Khondalite series, Huai'an complex, and Hengshan complex which are the subdivisions of metamorphic outburst classification (Wang et al., 2016). The temperature and pressure environment at a depth of 35–40 km at the bottom of the Paleoarchean lower crust is evidenced by the high pressure in the mafic granulites. The subduction–collision–exhumation events of Paleoproterozoic orogenic tectonic development transported these high-pressure granulites and eclogites into the core crust (Zhang et al., 2019).Geophysical methods can effectively understand the current deep structures and the

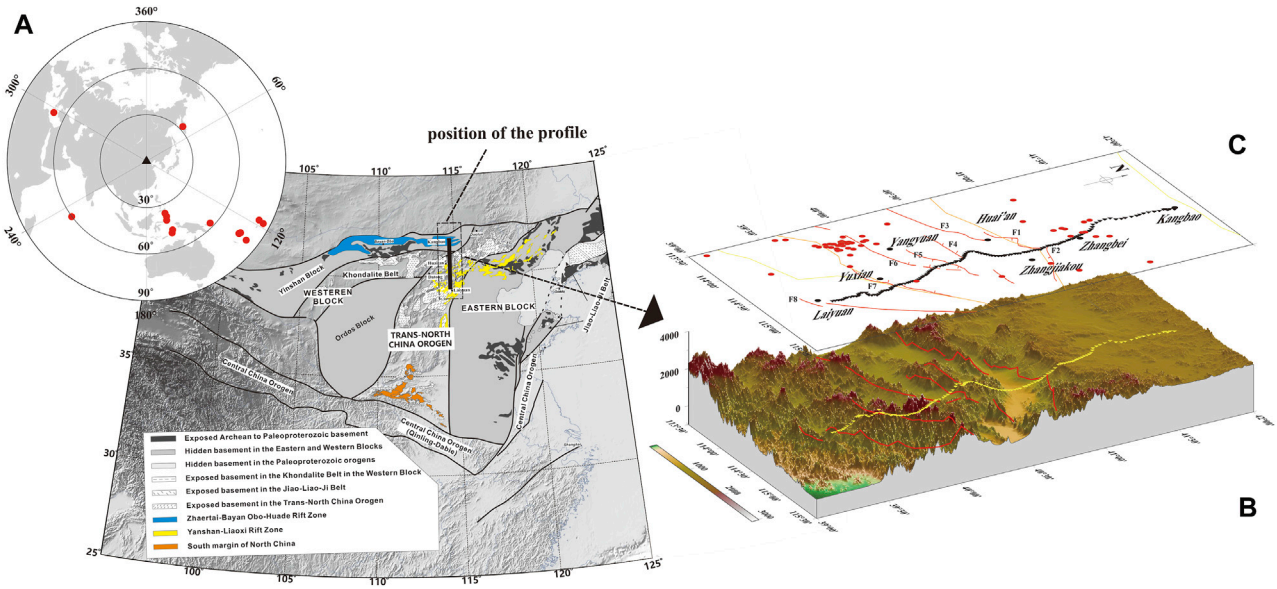

FIGURE 1
Geological background and the station map. **(A)** Integration of the North China Craton and the position of the profile (Zhao et al., 2012) and teleseismic events and station distribution. Red circles represent the events recorded, and the black triangle represents the center of the array; **(B)** spatial relationship between the topography, stations, Cenozoic fault distribution, and dense seismic array in the study area; **(C)** plane relationship between platform array and faults. The fault names are: F1-Huai'an–Wanquan Basin northern margin fault; F2-Zhangjiakou fault; F3-Tianzhen–Yanggao basin northern margin fault; F4-Huai'an Basin southern margin fault; F5-Yangyuan basin northern margin fault; F6-Liulengshan basin northern margin fault; F7-Yuguang basin southern margin fault; F9-Sunzhuangzi–Wulonggou fault; and F10-Xuanhua Basin southern margin fault.

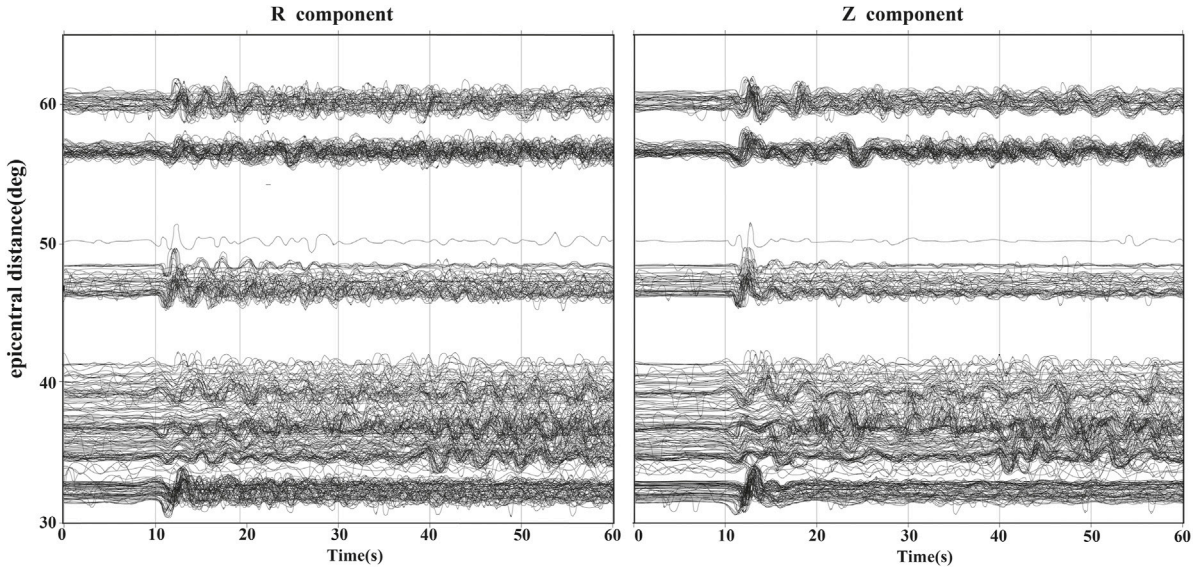

FIGURE 2
Observed teleseismic waveforms of R and Z components (after 0.02–2 Hz bandpass filtering).

tectonic processes. Several scholars have reported the strong concordance of surface topographic changes in the area and the E-W variations in the crustal and lithospheric structures (e.g., Chen, 2010; Cheng et al., 2013; Wei et al., 2015; Zheng et al., 2017). NCC and several other cratons in the world have restructured as a result of subduction (Zhu et al., 2021), and the pre-existing structures in the lithosphere primarily control such continental reconfiguration. However, deep imaging results of satisfactory scales in this local area are still lacking. In this context, the reconfiguration of the ancient tectonic amalgamation belt was investigated by procuring the higher precision imaging results of deep structures. For this purpose, a short-period array was deployed in the Huai'an-Zhangjiakou area to apply the receiver function method for exploring deep structures. The present tectonic activity explained the activation of the ancient tectonic structures based on the imaging results.

2 Method and data

2.1 Method

The receiver function is a reliable seismological method widely applied for the detection of discontinuities in the crust and upper mantle. This approach extracts the signatures of the structure under the station by the deconvolution of the R and Z directions of seismic wave records. The depth of the discontinuities, the crustal thickness, and the average velocity ratio of the crust can be estimated by analyzing the time and amplitude of the P-to-S wave of the crust or upper mantle discontinuities. This method is also used for the development of broadband seismology (Langston, 1979; Yuan et al., 1997; Zhu and Kanamori, 2000) and understanding the crustal and upper mantle structure globally and regionally with a multitude of intriguing conclusions. However, the distance between stations in broadband seismic array observation is generally more than 10 km, with longer periods of observation, typically several years, due to the constraints of observation cost and environment, which also limits its implementation. Apart from this, the spatial resolution is also limited due to the minimum distance of such stations' separation. However, this method has been successfully applied recently in dense array observation data for a shorter time period. In petroleum exploration, a dense array of stations are established flexibly and quickly at several hundred meters apart by the operation of low-cost and simple nodal seismographs. After a short period of continuous observation (1–2 months), suitable teleseismic earthquakes can be identified for high-resolution crustal structure imaging. Several studies have been successfully carried out globally on the investigation of short-period dense array observation data. For example, a series of innovative research studies have been performed in Long Beach (e.g., Lin et al., 2013; Bowden et al., 2015; Bianco et al., 2019), a representative study area where a shallow magma chamber was imaged under the Wudalianchi volcanic field using highly dense arrays (Li et al., 2016). Similarly, Wang et al. (2019) imaged the fault damage zone of the San Jacinto Fault near Anza using a dense array of ambient noise tomography. The unprecedented details of the growing crustal structure along various boundaries of the Tibetan Plateau were unveiled by a series of short-period dense arrays (e.g., Liu X et al., 2017; Shen et al., 2020, 2022; Tian et al., 2021). Furthermore, the existence of Paleoproterozoic residual subduction in the craton

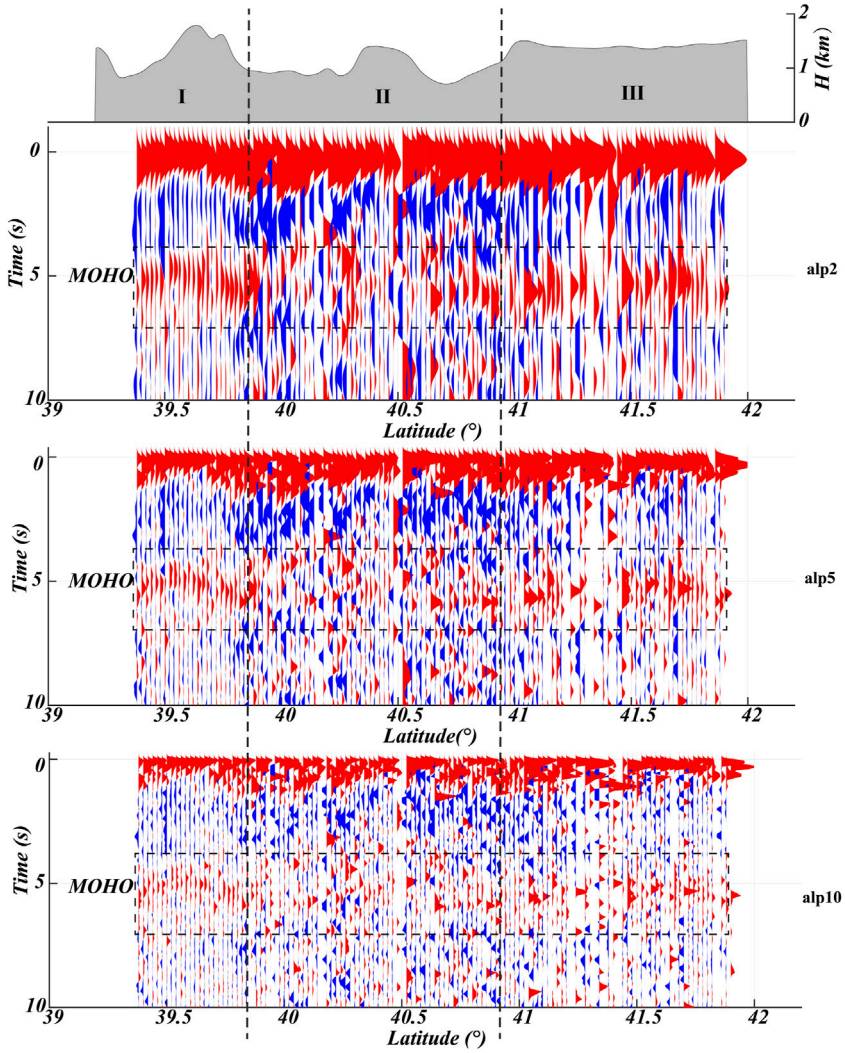

FIGURE 3
Stacking profile of receiver functions with different Gaussian filter factors (alp). Alp = 2 (1.18 s pulse width), 5 (0.75 s pulse width), and 10 (0.53 s pulse width) were used to compare the signal stability.

margin was revealed by deploying a high-density seismic array across the boundary between the Yinshan block and the Ordos block (the Khondalite belt) (Wan et al., 2020).

2.2 High dense seismic array and data source

From August 2020 to September 2020, we deployed approximately 230-km-long seismic profiles with 140 short-period seismometers, crossing the ancient tectonic boundary and rift system from south to north in our study area (Figure 1 b and c). EPS seismometers with a flat velocity response ranging from 0.2 to 200 Hz were kept nearly 1–3 km apart, and the observations were performed continuously for nearly one month with a sampling rate of 100 samples/s. The teleseismic waveform records of Ms > 5.5 with distinct P-wave signal onsets were carefully identified within an epicentral distance range of 30°–95° (Figure 1D). The earthquake catalog was obtained from the global United States Geological Survey (USGS) (http://neic.usgs.gov/neis/epic/epic_global.html), and the event waveforms with obvious P-wave onset signals are shown in Figure 2.

2.3 Data processing procedure

Each seismic event's theoretical p-wave arrival time was calculated based on the IASP91 model (Kennett and Engdahl,

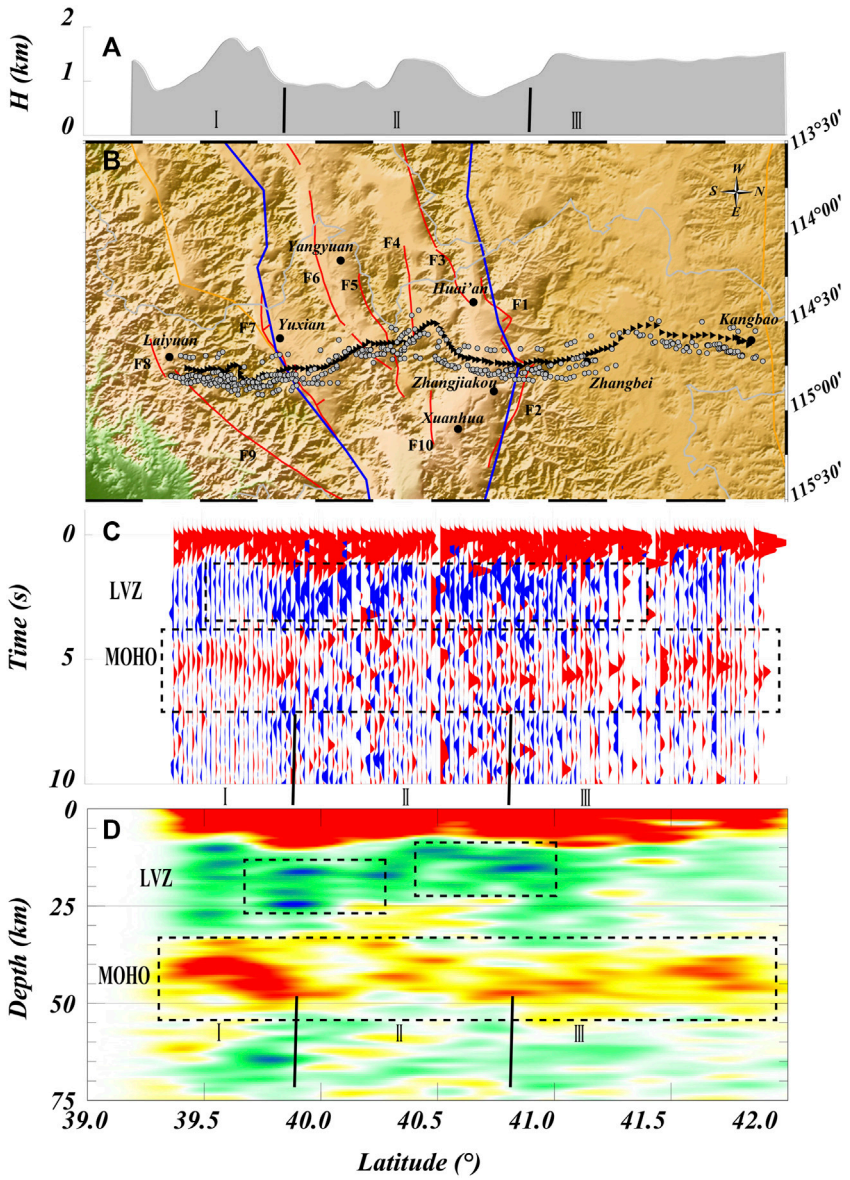

FIGURE 4
Topography, receiver function, and migration image. **(A)** Topographic elevation of the survey line, **(B)** topography and geomorphology of the study area and the distribution plan of the station, and **(C)** profile under the survey line superimposed by the receiving function. **(D)** CCP result. F1-Huai'an–Wanquan Basin northern margin fault; F2-Zhangjiakou fault; F3-Tianzhen–Yanggao basin northern margin fault; F4-Huai'an Basin southern margin fault; F5-Yangyuan basin northern margin fault; F6-Liulengshan basin northern margin fault; F7-Yuguang basin southern margin fault; F9-Sunzhuangzi–Wulonggou fault; F10-Xuanhua Basin southern margin fault.

1991). The seismic data between 20 s before and 80 s after the P-wave were collected after calibrating the P-wave arrival. Furthermore, the mean, the linear trend, and other filtering processes were removed to check the waveform quality. The original ENZ component data were rotated to the RTZ component per the circle path. The waveforms with relatively clear recorded events were deconvoluted with different Gaussian filters to obtain the receiver functions and subsequently selected the clear receiver functions of the PmS seismic phase (Ligorría and Ammon, 1999). A Gaussian filter of 5 with an approximate pulse width of 0.75 s was used to maintain the detailed information in receiver function traces. Also, the receiver functions with a Gaussian filter of 2 (1.18 s pulse width), 5 (0.75 s pulse width), and 10 (0.53 s pulse width) were calculated to test the stability of signal characteristics (Figure 3). The crustal structure under the station was

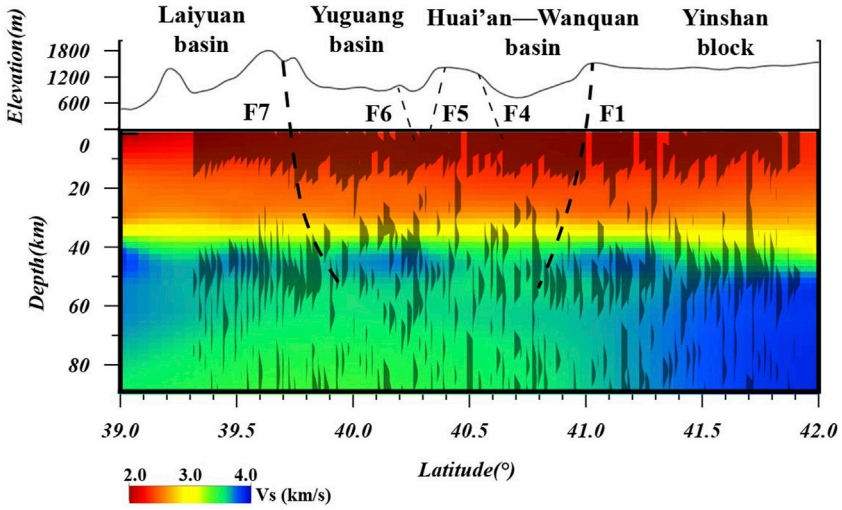

FIGURE 5
Tomography profile and receiver functions. The tomography results are combined with the results reported by Tao et al. (2018).

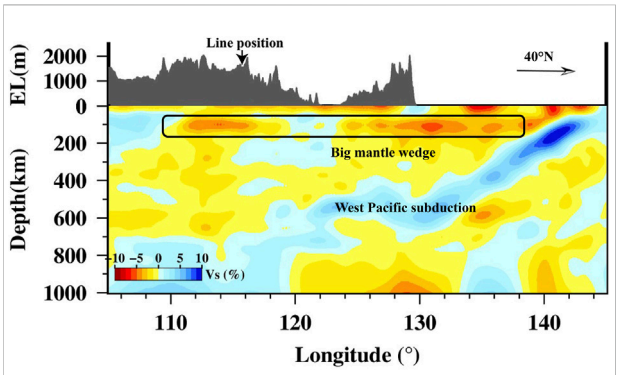

FIGURE 6
Tomographic profile of the Pacific subduction with latitude = 40°N (according to Tao et al., 2018)

obtained by stacking in accordance with the transition point of projection and subsequently selected 560 high-quality receiver functions. The influence of other interfaces at different epicentral distances was reduced by correcting the time of receiver functions with P-to-S moveout correction by setting a reference distance of 65° and a focal length of 20 km. Thus, the receiver functions may be configured to display the undulations of the Moho or the interfacial features of the crust. The profiles of stacking receiver functions after P-to-S moveout correction during different periods along the longitude of PmS pierce points, calculated based on the IASP91 model, are shown in Figure 3.

Furthermore, the receiver functions on the temporal domain were converted into the spatial domain along the ray path and P-to-S conversion arrivals by the common conversion point (CCP) stacking method (Yuan et al., 1997). For migration purposes, the crust and upper mantle within 75 km depth were divided into 0.5 km segments in both the horizontal and vertical directions, and subsequently, the quality of migration images was improved by staking the receiver functions with the pierce points along the ray path using the IASP91 model to generate the final migration images ultimately. The migration images obtained along the profiles from receiver functions with the Gaussian filter of 5 are shown in Figure 4D.

3 Results

The reliable signals in the receiver functions are stable with variations in time and alp. A smaller alp factor provides the Moho basic and smoothed interface data, while a larger alp factor provides more crustal information (Wei et al., 2016). Even though the signal of the Moho is about 5 s (depth of approximately 40 km), it has a distinct segmented pattern from south to north. The profile is subdivided into three characteristic segments based on the shape of the Moho signal: (I) 39°N–39.8°N (south of F7), where the Moho is clear and continuous in the staking profile, gradually descending from south to north; (II) 39.8°N–40.7°N (between F7 and F1), where the morphology is complex with weak continuity, exhibiting no single layer; and (III) 40.7°N–42°N (north of F1), where the Moho is relatively stable and flat. In addition, some relatively stable negative signals shallower than 25 km depth observed in the range of

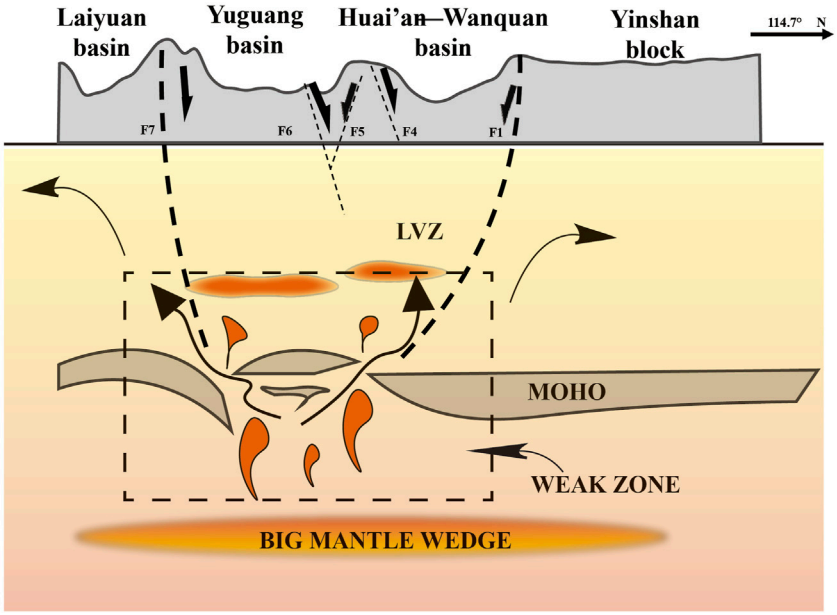

FIGURE 7
Sketched model of the interaction between the mantle and crust.

36.7°N–41.5°N may represent a low-velocity zone (LVZ) within the crust. A comparative analysis of topographic elevation, surface structure, receiver function results, and CCP results are shown in Figure 4. Based on the CCP results, the Moho exhibits a uniform pattern. However, the Moho in region I is curved downward, while that in region II is relatively complex and that in region III is relatively flat. The LVZ is mainly concentrated in region II and is discontinuous. The complex features of the Moho represent a series of surfaces closely related to structural features and deep structures and are visible below the densely constructed basin ridges.

4 Discussion

NCC is regarded as the most severely damaged craton on earth (Carlson et al., 2005; Zhu et al., 2011). The tectonic belts around cratons are relatively mechanically weak zones compared to the cratons and are primary sites of intense heating and strain localization (Hu et al., 2018; Liu et al., 2021). Based on the imaging results, the average depth of the Moho beneath the profile is 40 km. A comparative study was carried out on the basic crustal conditions under the adjacent regions in North China by the receiver function method and by using the broadband seismograph data (Zheng et al., 2007; Chen, 2009; Tang et al., 2010; Lou et al., 2017; Si et al., 2017; Wei et al., 2020; Zuo et al., 2020), which are comparable with crustal thickness obtained by the measured receiver functions. The imaging results of the Moho obtained from region I and region III are comparable to the results from the western Khondalite belt (Wan et al., 2020). Moreover, the results of wide-angle reflection and refraction profile data of deep seismic sounding indicate the existence of a deep crust-scale fault zone extending to the Moho beneath the Zhangjiakou area, as well as the presence of LVZ within the crust (Zhu et al., 1999), which may suggest the presence of intense magmatic activity.

Numerical experiments demonstrate that inheritance is the primary controlling factor of lithospheric rifting and layer stiffness. The rift styles mostly depend on the inherited weaknesses embedded in the model (Chenin and Beaumont, 2013). The study area crosses through Yuguang and Wanquan basins from south to north and crosses a series of Holocene normal faults, making the area active. The normal faults are distributed in the east of the western parts, and their characteristic stress conditions are generally in a north–south extensional environment. On the other hand, the combined analysis of previous tomographic results using the receiver function shows that the Moho in region II is discontinuous (Figure 5). Also, the complex deep structure in region II corresponds rather well with the distribution of the faults and basins, implying that the surface topography variation is generally congruent with the deep dynamic processes. Faults 1 and 7 seem to represent two boundaries of the whole fault and basin system, governed by the migration

of deep material on both sides. Frequently, the axis of lithosphere extension and continental breakup is parallel to the orogenic belts and suture zones (van Wijk, 2005). This area is probably related to the weak zone formed by the collage of Yinshan and Ordos blocks, which is evidenced by the combined analysis of the area with the E-W trend of the surface structure.

F1-Huai'an–Wanquan Basin northern margin fault; F4-Huai'an Basin southern margin fault; F5-Yangyuan basin northern margin fault; F6-Liulengshan basin northern margin fault; F7-Yuguang basin southern margin fault.

Based on the tomography results, subduction of the western Pacific has extended westward into the central and WNCC toward the Datong volcano (Wei et al., 2012; Liu Z et al., 2017; Zhao, 2017; Lei et al., 2018), with a large mantle wedge in the middle and upper mantle. The depth profile of the S-wave perturbation velocity along the latitude of 40°N is illustrated in Figure 6 based on the topography results reported by Tao et al. (2018).

The Pacific plate is deeply subducted toward the west, forming a large mantle wedge, and its influence extends westward, up to a longitude of 110°E. The uneven mantle flow in the upper mantle caused by the subducting slab front poses strong action on the upper lithosphere, thereby influencing the tectonic evolution of the crustal and upper mantle structure beneath NC (Tian et al., 2019). The high calorific value in North China at a depth of ~100 km is also evidenced by the geothermal results reported by Wang and Cheng, (2012). The low-velocity anomalies in the crust and upper mantle below the Zhangjiakou area are shown by the local ambient noise (Jiang et al., 2021). The aforementioned findings show that certain Cenozoic tectonic deformation and fault development in the study area are strongly connected to the internal restructuring of the craton caused by the subduction of the western Pacific plate. The area is tectonically characterized by the western subduction of the Pacific plate and the distinct local restructuring evidenced by the formation of a large mantle wedge. The tomography images from ambient noise also reveal that the crust and upper mantle beneath the Shanxi fault depression belt, Zhangjiakou, and Datong volcanic areas are characterized by low-velocity anomalies associated with a large area of intense Cenozoic magmatic activity in Datong triggered by the upwelling of hot materials from the mantle (Zuo et al., 2020), and the slow movement of the magma surface causing negative signals.

LVZ-low-velocity zone; F1-Huai'an–Wanquan Basin northern margin fault; F4-Huai'an Basin southern margin fault; F5-Yangyuan basin northern margin fault; F6-Liulengshan basin northern margin fault; F7-Yuguang basin southern margin fault.

The results of the receiver function and tomographic imaging were combined to generate a conceptual diagram of the tectonic process of this area, as shown in Figure 7. Since region II in Figure 3 and Figure 4 was relatively weak in the ancient craton collage belt earlier, it is more sensitive to get impacted by the mantle wedge (Zuo et al., 2020). These weak zones are reactivated by the mantle plume resulting in the upwelling of the Moho as channels, which ultimately restructures the crust. The shallow crust's materials are pushed to move on both sides by the circulatory power of deep materials, resulting in a series of normal faults and grabens on the earth's surface. As a result, region I and region III may still retain the shape of the ancient Moho without substantial changes.

5 Conclusion

In the present study, a short-period dense array is used to generate the receiver function image of two ancient tectonic belt boundaries of NCC. The extensive continental restructuring of the area might have affected the structure and properties of the continental lithosphere and impacted both surface processes and mantle dynamics regionally. For example, the series of nearly parallel E-W basins and lithospheric scale normal faults in the study area demonstrate their relationship with the pre-existing weak zone apart from the signatures representing current tectonic processes. The present study proposed a model illustrating the damage of the ancient weak zone caused by the dynamic processes of western Pacific subduction. The mantle wedge activates the local thermal circulation in the lithosphere to reactivate the weak zone to enter the crust as a channel which forms an extensional environment. This is evidenced by the slowly cooling magma upwelling of LVZ at the bottom of the upper crust in Zhangbei-Huai'an and Yangyuan basins.

Data availability statement

The original contributions presented in the study are included in the article/Supplementary Material; further inquiries can be directed to the corresponding author.

Author contributions

Conception and design of the study: QZ and XS; acquisition of data: QZ and XS; analysis and/or interpretation of the data: QZ, XS, HH, SC, and JZ; drafting the manuscript: QZ and XS; revising the manuscript critically for important intellectual

content: QZ.

Funding

Some figures are plotted using the Generic Mapping Tools (Wessel et al., 2019). This study was financially supported by the National Key Research and Development Program of China (2017YFC1500100), the National Natural Science Foundation of China (Grant Nos. 41874052 and 41730212), the Second Tibetan Plateau Scientific Expedition and Research Program (STEP) (2019QZKK0701), the Guangdong Province Introduced Innovative R&D Team (2016ZT06N331 and 2017ZT07Z066), and the Guangdong Collaborative Innovation Center for Earthquake Prevention and Mitigation (2018B020207011).

Conflict of interest

The authors declare that the research was conducted in the absence of any commercial or financial relationships that could be construed as a potential conflict of interest.

Publisher's note

All claims expressed in this article are solely those of the authors and do not necessarily represent those of their affiliated organizations, or those of the publisher, the editors, and the reviewers. Any product that may be evaluated in this article, or claim that may be made by its manufacturer, is not guaranteed or endorsed by the publisher.

References

Bianco, M. J., Gerstoft, P., Olsen, K. B., and Lin, F. (2019). High-resolution seismic tomography of Long Beach, CA using machine learning. *Sci. Rep.* 9, 14987. doi:10.1038/s41598-019-50381-z

Bowden, D., Tsai, V., and Lin, F. (2015). Site amplification, attenuation, and scattering from noise correlation amplitudes across a dense array in Long Beach, CA. *Geophys. Res. Lett.* 42, 1360–1367. doi:10.1002/2014gl062662

Carlson, R. W., Pearson, D. G., and James, D. E. (2005). Physical, chemical, and chronological characteristics of continental mantle. *Rev. Geophys* 43, G1001. doi:10.1029/2004rg000156

Chen, L. (2010). Concordant structural variations from the surface to the base of the upper mantle in the North China Craton and its tectonic implications. *Lithos* 120, 96–115. doi:10.1016/j.lithos.2009.12.007

Chen, L. (2009). Lithospheric structure variations between the eastern and central North China Craton from S- and P-receiver function migration. *Phys. Earth Planet. Interiors* 173, 216–227. doi:10.1016/j.pepi.2008.11.011

Cheng, C., Chen, L., Yao, H., Jiang, M., and Wang, B. (2013). Distinct variations of crustal shear wave velocity structure and radial anisotropy beneath the North China Craton and tectonic implications. *Gondwana Res.* 23, 25–38. doi:10.1016/j.gr.2012.02.014

Chenin, P., and Beaumont, C. (2013). Influence of offset weak zones on the development of rift basins: Activation and abandonment during continental extension and breakup. *JGR. Solid Earth* 118 (4), 1698–1720. doi:10.1002/jgrb.50138

Hu, J., Liu, L., Faccenda, M., Zhou, Q., Fischer, K. M., Marshak, S., et al. (2018). Modification of the Western Gondwana craton by plume-lithosphere interaction. *Nat. Geosci.* 11, 203–210. doi:10.1038/s41561-018-0064-1

Jiang, L., Ding, Z., Gao, T., and Huang, X. (2021). Crustal structure beneath the North China Craton from joint inversion of ambient noise and receiver function. *Chin. J. Geophys.* 64 (5), 1585–1596. (In Chinese). doi:10.6038/cjg2021O0144

Kennett, B. L. N., and Engdahl, R. (1991). Travel times for global earthquake location and phase identification. *Geophys. J. Int.* 105, 429–465. doi:10.1111/j.1365-246X.1991.tb06724.x

Kusky, T. M., Polat, A., Windley, B. F., Burke, K. C., Dewey, J. F., Kidd, W. S. F., et al. (2016). Insights into the tectonic evolution of the North China Craton through comparative tectonic analysis; a record of outward growth of Precambrian continents. *Earth. Sci. Rev.* 162, 387–432. doi:10.1016/j.earscirev.2016.09.002

Langston, C. A. (1979). Structure under Mount Rainier, Washington, inferred from teleseismic body waves. *J. Geophys. Res.* 84, 4749–4762. doi:10.1029/jb084ib09p04749

Lei, J., Zhao, D., Xu, Y., Fan, Q., Mi, Q., Du, M., et al. (2018). Is there a gap in the stagnant Pacific slab in the mantle transition zone under the Changbaishan volcano? *Acta Petrol. Sin. Chin.* 34 (1), 13–22.

Li, S., Li, X., Dai, L., Liu, X., Zhang, Z., Zhao, S., et al. (2015). Precambrian geodynamics(VI):formation of north China craton. *Earth Sci. Front.* 22, 77–96. in chinese.

Li, Z., Ni, S., Zhang, B., Bao, F., Zhang, S., Deng, Y., et al. (2016). Shallow magma chamber under the Wudalianchi Volcanic Field unveiled by seismic imaging with dense array. *Geophys. Res. Lett.* 43, 4954–4961. doi:10.1002/2016gl068895

Li, Z., Qu, H., and Gong, W. (2015). Late Mesozoic basin development and tectonic setting of the northern North China Craton. *J. Asian Earth Sci.* 114, 115–139. doi:10.1016/j.jseaes.2015.05.029

Ligorría, J. P., and Ammon, C. (1999). Iterative deconvolution and receiver function estimation. *Bull. Seismol. Soc. Am.* 5, 1395–1400. doi:10.1785/bssa0890051395

Lin, F., Li, D., Clayton, R., and Hollis, D. (2013). High-resolution 3D shallow crustal structure in Long Beach, California: Application of ambient noise tomography on a dense seismic array. *Geophysics* 78, Q45–Q56. doi:10.1190/geo2012-0453.1

Liu, J., Pearson, D., Wang, L., Mather, K., Kjarsgaard, B., Schaeffer, A., et al. (2021). Plume-driven recratonization of deep continental lithospheric mantle. *Nature* 592 (7856), 732–736. doi:10.1038/s41586-021-03395-5

Liu, X., Zhao, D., Li, S., and Wei, W. (2017). Age of the subducting Pacific slab beneath East Asia and its geodynamic implications. *Earth Planet. Sci. Lett.* 464, 166–174. doi:10.1016/j.epsl.2017.02.024

Liu, Z., Tian, X., Gao, R., Wang, G., Wu, Z., Zhou, B., et al. (2017). New images of the crustal structure beneath eastern Tibet from a high-density seismic array. *Earth Planet. Sci. Lett.* 480, 33–41. doi:10.1016/j.epsl.2017.09.048

Lou, X., Ai, Y., Zhang, Y., Chen, Y., and Ning, J. (2017). Study of lithospheric structure in the central and western north China craton. *Prog. Geophys. (in Chinese)* 32 (4), 1458–1464. doi:10.6038/pg20170406

Shen, X., Li, Y., Gao, R., Chen, X., Liu, M., Yuan, X., et al. (2020). Lateral growth of NE Tibetan Plateau restricted by the Asian lithosphere: Results from a dense seismic profile. *Gondwana Research* 87, 238–247. doi:10.1016/j.gr.2020.06.018

Shen, X., Zhou, Q., Cheng, S., Zheng, W., Zhang, P., Zhang, D., et al. (2022). Contrasting crustal structures crossing the boundary region of the southwest Ordos block and its tectonic implications revealed by dense seismic arrays. *Tectonophysics* 831, 229342. doi:10.1016/j.tecto.2022.229342

Si, S., Tian, X., and Gao, R. (2017). Constraints on upper mantle Vp/Vs ratio variations beneath eastern North China from receiver function tomography. *J. Asian Earth Sci.* 138, 341–356. doi:10.1016/j.jseaes.2017.02.025

Tang, Y., Feng, Y., Chen, Y., Zhou, S., Ning, J., Wei, S., et al. (2010). Receiver function analysis of Shanxi rift. *Chinese Geophys* 53 (9), 2102–2109. (in Chinese). doi:10.3969/j.issn.0001-5733.2010.09.01

Tao, K., Grand, S. P., and Niu, F. (2018). Seismic structure of the upper mantle beneath eastern asia from full waveform seismic tomography. *Geochem. Geophys. Geosyst.* 19, 2732–2763. doi:10.1029/2018gc007460

Tian, X., Bai, Z., Simon, L. K., Liang, X., Liu, Z., Wang, X., et al. (2021). Crustal-scale wedge tectonics at the narrow boundary between the Tibetan Plateau and Ordos block. *Earth Planet. Sci. Lett.* 554, 116700. doi:10.1016/j.epsl.2020.116700

Tian, Y., Ma, J., Liu, C., Feng, X., Liu, T., Zhu, H., et al. (2019). Effects of subduction of the Western Pacific plate on tectonic evolution of Northeast China

and geodynamic implications. *Chinese Journal of Geophysics (in Chinese)* 62 (3), 1071–1082. doi:10.6038/cjg2019M0061

van Wijk, J. W. (2005). Role of weak zone orientation in continental lithosphere extension. *Geophys. Res. Lett.* 32 (2), L02303. doi:10.1029/2004gl022192

Wan, B., Yang, X., Tian, X., Yuan, H., Kirscher, U., and Mitchell, R. N. (2020). Seismological evidence for the earliest global subduction network at 2 Ga ago. *Sci. Adv.* 6, c5491. doi:10.1126/sciadv.abc5491

Wang, H., Zhang, H., Zhai, M., Oliveira, E. P., Ni, Z., Zhao, L., et al. (2016). Granulite facies metamorphism and crust melting in the Huai'an terrane at~1.95Ga, North China Craton: New constraints from geology, zircon U–Pb, Lu–Hf isotope and metamorphic conditions of granulites. *Precambrian Res.* 286, 126–151. doi:10.1016/j.precamres.2016.09.012

Wang, Y., Allam, A., and Lin, F. C. (2019). Imaging the fault damage zone of the san Jacinto Fault near Anza with ambient noise tomography using a dense nodal array. *Geophys. Res. Lett.* 46, 12938–12948. doi:10.1029/2019gl084835

Wang, Y., and Cheng, S. (2012). Lithospheric thermal structure and rheology of the eastern China. *J. Asian Earth Sci.* 47, 51–63. doi:10.1016/j.jseaes.2011.11.022

Wei, W., Xu, J., Zhao, D., and Shi, Y. (2012). East Asia mantle tomography: New insight into plate subduction and intraplate volcanism. *J. Asian Earth Sci.* 60, 88–103. doi:10.1016/j.jseaes.2012.08.001

Wei, Z., Chen, L., Li, Z., Ling, Y., and Li, J. (2016). Regional variation in Moho depth and Poisson's ratio beneath eastern China and its tectonic implications. *J. Asian Earth Sci.* 115, 308–320. doi:10.1016/j.jseaes.2015.10.010

Wei, Z., Chu, R., and Chen, L. (2015). Regional differences in crustal structure of the North China Craton from receiver functions. *Sci. China Earth Sci.* 58, 2200–2210. doi:10.1007/s11430-015-5162-y

Wei, Z., Li, Z., Chen, L., Chu, R., Wu, S., Ling, Y., et al. (2020). Crustal structure underneath central China across the Tibetan Plateau, the North China Craton, the South China Block and the Qinling-Dabie Orogen constrained by multifrequency receiver function and surface wave data. *J. Asian Earth Sci.* 202, 104535. doi:10.1016/j.jseaes.2020.104535

Wessel, P., Luis, J. F., Uieda, L., Scharroo, R., Wobbe, F., Smith, W. H. F., et al. (2019). The generic mapping Tools version 6. *Geochem. Geophys. Geosyst.* 20, 5556–5564. doi:10.1029/2019gc008515

Wu, Y., Li, L., Chen, C., Liang, H., Guo, N., and Li, Y. (2021). GNSS deformation characteristics of North China in the past two decades. *Geodesy and Geodynamics* 12, 392–398. doi:10.1016/j.geog.2021.08.004

Yang, Z., Chen, Y., and Zhang, H. (2002). Relocation and seismogenic structure of the 1998 Zhangbei-Shangyi earthquake sequence. *Acta Seimol. Sin.* 15, 383–394. doi:10.1007/s11589-002-0031-0

Yuan, X., Ni, J. F., Kind, R., Mechie, J., and Sandvol, E. (1997). Lithospheric and upper mantle structure of southern Tibet from a seismological passive source experiment. *J. Geophys. Res.* 102, 27491–27500. doi:10.1029/97jb02379

Zhai, M., and Santosh, M. (2011). The early precambrian odyssey of the north China craton: A synoptic overview. *Gondwana Research* 20, 6–25. doi:10.1016/j.gr.2011.02.005

Zhang, J., Wang, H., Tian, H., Ren, Y., Chang, Q., Shi, J., et al. (2019). Petrogenesis of the MORB type highpressure mafic granulite from the Huai'an complex in North China Craton and its tectonic implications. *Acta Petrologica Sinica* 35 (11), 3506–3528. doi:10.18654/1000-0569/2019.11.16

Zhao, D. (2017). Big mantle wedge, anisotropy, slabs and earthquakes beneath the Japan Sea. *Physics of the Earth and Planetary Interiors* 270, 9–28. doi:10.1016/j.pepi.2017.06.009

Zhao, G., Cawood, P. A., Li, S., Wilde, S. A., Sun, M., Zhang, J., et al. (2012). Amalgamation of the north China craton: Key issues and discussion. *Precambrian Res.* 222-223, 55–76. doi:10.1016/j.precamres.2012.09.016

Zhao, G., Sun, M., Wilde, S. A., and Li, S. (2005). Late archean to paleoproterozoic evolution of the north China craton: Key issues revisited. *Precambrian Res.* 136, 177–202. doi:10.1016/j.precamres.2004.10.002

Zhao, G., Wilde, S. A., Cawood, P. A., Sun, M., Cruden, A. R., and Easton, R. M. (2001). Archean blocks and their boundaries in the North China Craton; lithological, geochemical, structural and P-T path constraints and tectonic evolution. *Precambrian Res.* 107, 45–73. doi:10.1016/s0301-9268(00)00154-6

Zhao, G., Zhai, M., Zheng, Y., Xiao, W., and Zhao, G. (2013). Lithotectonic elements of Precambrian basement in the North China Craton; review and tectonic implications. *Gondwana Research* 23, 1207–1240. doi:10.1016/j.gr.2012.08.016

Zheng, T., Chen, L., Zhao, L., and Zhu, R. (2007). Crustal structure across the Yanshan belt at the northern margin of the North China Craton. *Physics of the Earth and Planetary Interiors* 161, 36–49. doi:10.1016/j.pepi.2007.01.004

Zheng, T., Duan, Y., Xu, W., and Ai, Y. (2017). A seismic model for crustal structure in North China Craton. *Earth and Planetary Physics* 1, 26–34. doi:10.26464/epp2017004

Zhu, L., and Kanamori, H. (2000). Moho depth variation in southern California from teleseismic receiver functions. *J. Geophys. Res.* 105, 2969–2980. doi:10.1029/1999jb900322

Zhu, R., Chen, L., Wu, F., and Liu, J. (2011). Timing, scale and mechanism of the destruction of the North China Craton. *Sci. China Earth Sci.* 54, 789–797. doi:10.1007/s11430-011-4203-4

Zhu, R., Yang, J., and Wu, F. (2012). Timing of destruction of the north China craton. *Lithos* 149, 51–60. doi:10.1016/j.lithos.2012.05.013

Zhu, R., Zhao, G., Xiao, W., Chen, L., and Tang, Y. (2021). Origin, accretion, and reworking of continents. *Rev. Geophys.* 59. doi:10.1029/2019rg000689

Zhu, Z., Zhang, J., Zhang, X., Zhang, C., and Liu, M. (1999). The crust-mantle structure in zhangbei-shangyi earthquake area. *Earthquake Reserch IN China(in Chinese)* 15 (1), 68–76.

Zuo, J., Wang, L., and Niu, F. (2020). Multiple source downwellings beneath eastern North China revealed by 3-D CCP migration of receiver function data. *J. Asian Earth Sci.* 192, 104266. doi:10.1016/j.jseaes.2020.104266